

GIANT H II REGIONS IN M101. I. X-RAY ANALYSIS OF HOT GAS

WEI SUN¹, YANG CHEN^{1,2,6}, LI FENG¹, YOU-HUA CHU³, C.-H. ROSIE CHEN⁴, Q. DANIEL WANG⁵, JIANG-TAO LI^{2,5}

Draft version October 9, 2012

ABSTRACT

We performed a *Chandra* X-ray study of three giant H II regions (GHRs), NGC 5461, NGC 5462, and NGC 5471, in the spiral galaxy M101. The X-ray spectra of the three GHRs all contain a prominent thermal component with a temperature of ~ 0.2 keV. In NGC 5461, the spatial distribution of the soft (< 1.5 keV) X-ray emission is generally in agreement with the extent of H1105, the most luminous H II region therein, but extends beyond its southern boundary, which could be attributed to outflows from the star cloud between H1105 and H1098. In NGC 5462, the X-ray emission is displaced from the H II regions and a ridge of blue stars; the H α filaments extending from the ridge of star cloud to the diffuse X-rays suggest that hot gas outflows have occurred. The X-rays from NGC 5471 are concentrated at the B-knot, a “hypernova remnant” candidate. Assuming a Sedov-Taylor evolution, the derived explosion energy, on the order of 10^{52} ergs, is consistent with a hypernova origin. In addition, a bright source in the field of NGC 5462 has been identified as a background AGN, instead of a black hole X-ray binary in M101.

Subject headings: Galaxies: individual (M101) – H II regions – ISM: bubbles – ISM: kinematics and dynamics – X-rays: ISM

1. INTRODUCTION

Intense star formation and subsequent evolution of massive stars are spectacular processes observable from radio through optical to X-ray and even γ -ray wavelengths, and represent a microcosm of starburst astrophysics. Upon formation from giant molecular clouds, young massive stars emit large amounts of ultraviolet (UV) radiation to ionize the ambient medium into H II regions. The accumulated kinetic energy injected by stellar winds from O-type and Wolf-Rayet stars rival the explosion energies of supernovae (SNe). These mechanical energies not only shock-heat the ambient medium to 10^6 – 10^8 K that emits diffuse X-rays, but also may compress ambient clouds to trigger further star formation. Within this medium, newly formed X-ray binaries and magnetized young stellar objects shine as point sources in X-rays. Regions of massive star formation are thus excellent astrophysical laboratories to study the co-evolution of massive stars and the multi-phase interstellar medium.

Giant H II regions (GHRs) are sites of intense star formation qualified as starbursts. Their H α luminosities, typically $\sim 10^{39}$ – 10^{41} erg s^{−1} (Kennicutt 1984), require an ionizing power equivalent to that of 24–2400 O5V stars (Schaerer & de Koter 1997). Depending on their stellar content and interstellar environments, GHRs may possess very different X-ray properties. 30 Doradus (30 Dor) in the Large Magellanic Cloud (LMC) is dominated by a central massive cluster, R136 (Feast et al. 1960) with

a mass of $\sim 6 \times 10^4 M_{\odot}$ (Brandl 2005), and its diffuse X-ray luminosity is $L_X \simeq 1.4 \times 10^{37}$ erg s^{−1} in 0.5–8 keV (Wang 1999b; Townsley et al. 2006). NGC 604 in M33 contains multiple OB associations spreading over a large area (Hunter et al. 1996), and its hot ionized medium (HIM) has a total unabsorbed X-ray luminosity of 1.43×10^{36} erg s^{−1} (Tüllmann et al. 2008). IC 131, another GHR in M33, shows diffuse X-ray emission within a large shell southeast to a concentration of OB stars and the diffuse X-ray emission is characterized by an unusually hard spectrum (Tüllmann et al. 2009).

The generation of X-ray-emitting hot gas reflects the star formation activities and the accompanied high energy processes. We have chosen to study the GHRs NGC 5461, NGC 5462, and NGC 5471 in M101 at a distance of 6.8 Mpc (Saha et al. 2006, hence $1'' = 33$ pc), because they are several times as luminous as 30 Dor and exhibit contrasting optical morphologies (Chen et al. 2005), allowing us to investigate the generation and distribution of hot gas of GHRs with larger-scale starbursts.

NGC 5461 is a large ($40'' \times 25''$) H II complex with multiple components (Hodge et al. 1990). The linear size of NGC 5461 is ~ 1.3 kpc \times 0.82 kpc. Six R136-class clusters of quite young ages (< 5 Myr) have been identified by Chen et al. (2005); five of them are located in H1105, the main body of NGC 5461. It is suggested that the entire region is associated with two generations of star formation events (Pellerin 2006).

The GHR NGC 5462 corresponds to another large H II complex spreading $48'' \times 33''$, or ~ 1.6 kpc \times 1.1 kpc, as seen in ground-based H α images (Israel et al. 1975). Thirty-three H II regions are identified within NGC 5462 (Hodge et al. 1990), but none of them is comparable to 30 Dor (~ 290 pc \times 290 pc). Chen et al. (2005) have identified 25 cluster candidates in NGC 5462 and made photometric measurements; the two most luminous clusters have masses of $\sim 2 \times 10^4 M_{\odot}$ and ages of $\gtrsim 10$ Myr. At such ages, SNe explosions of massive stars begin to dom-

¹ Department of Astronomy, Nanjing University, Nanjing 210093, China

² Key Laboratory of Modern Astronomy and Astrophysics, Nanjing University, Ministry of Education, China

³ Department of Astronomy, University of Illinois, 1002 West Green Street, Urbana, IL 61801

⁴ Max Planck Institut für Radioastronomie, Auf dem Hügel 69, 53121 Bonn, Germany

⁵ Department of Astronomy, University of Massachusetts, Amherst, MA 01003, USA

⁶ Author to whom any correspondence should be addressed.

TABLE 1
JOURNAL OF ANALYZED *Chandra* ACIS OBSERVATION

ObsID	Start Date	Exposure (ks) ^a	CCD chips ^b				
			NGC 5461	NGC 5462	NGC 5471	Src. 6 ^c	Data Mode
2779	02.Oct.31	11.9	S3	S2	VFAINT
2065	00.Oct.29	9.63	...	S2	S2	S2	FAINT
4737	04.Jan.01	20.5	S3	S3	...	S3	VFAINT
4731	04.Jan.19	55.8	S2	...	VFAINT
5297	04.Jan.25	18.7	S2	...	VFAINT
5322	04.May.03	64.7	S2	VFAINT
4733	04.May.07	23.6	S2	VFAINT
5323	04.May.09	42.5	S2	VFAINT
4736	04.Nov.01	73.9	S2	S2	S2	S2	VFAINT
6152	04.Nov.07	22.7	S2	S2	S2	S2	VFAINT
6170	04.Dec.22	43.4	S3	S3	S2	S3	VFAINT
6175	04.Dec.24	40.6	S3	S3	S2	S3	VFAINT
6169	04.Dec.30	28.0	S3	S3	...	S3	VFAINT

^a Effective exposure, in which deadtime and bad time intervals due to flaring have been excluded.

^b CCD chips that contain the specific targets in the ACIS observations. The ellipses indicate observations not used.

^c A point source detected in NGC 5462. See Table 2 for details.

inate the energetics of the GHRs (Oskinova 2005). If the resulting hot gas is confined therein, the GHRs may be expected to be luminous X-ray sources.

NGC 5471 is a GHR in the outskirts of M101. Skillman (1985) identified five bright knots in NGC 5471 and concluded that the B-knot (NGC 5471B) contains a supernova remnant (SNR) because of its non-thermal radio emission and high [S II]/H α ratio. This SNR was subsequently suggested to be a “hypernova remnant” because its $\sim 10^{52}$ ergs explosion energy derived from the *ROSAT* X-ray observation was much higher than the canonical SN explosion energy 10^{51} ergs (Wang 1999a). NGC 5471B has been observed to be a large-velocity-width source (LVWS, Chu & Kennicutt 1986), which is unique among NGC 5461, NGC 5462, and NGC 5471 (Yang et al. 1994). In a follow-up critical examination of NGC 5471B, Chen et al. (2002) analyzed the underlying stellar population and the spectral and kinematic properties of the nebula, and concluded that these optical observations support the presence of a hypernova remnant in NGC 5471B.

To carry out a comprehensive investigation of the physical properties of multi-phase gas and evolving processes in these GHRs, we have examined *Chandra* X-ray observations and obtained H α echelle spectral mapping of NGC 5461 and NGC 5471 with the 4m Mayall Telescope at Kitt Peak National Observatory (KPNO). We report the analysis of hot gas in NGC 5461, NGC 5462, and NGC 5471 in this paper, and the kinematics of warm ionized gas in these GHRs in an upcoming paper. This paper is organized as follows: observations and data reductions are described in Section 2, the results of our analysis are presented in Section 3, the nature of the GHRs is discussed in Section 4, and conclusions are given in Section 5.

2. OBSERVATIONS AND DATA REDUCTIONS

The main data sets used in this study are from the archive of the *Chandra X-ray Observatory* observations. Archival data from the *Hubble Space Telescope* (*HST*), *Spitzer Space Telescope* and *Galaxy Evolution Explorer*

(*GALEX*) are also employed here for multi-wavelength comparisons.

The X-ray data analyzed here consist of several segments from the 1 Ms *Chandra* observation of M101 (Kuntz & Snowden 2010) and a 15 ks *Chandra* ACIS observation aimed at NGC 5471 (ObsID: 2779, PI: Q. D. Wang). The Ms observation is used for imaging and spectral analyses of NGC 5461 and NGC 5462. NGC 5471 is located at $\sim 20'$ off the aim point of the Ms observation of M101, where the 90% energy-encircled radius (EER) is greater than $15''$ for a point source⁷; therefore, only the 15 ks observation directly aimed at NGC 5471 is used to construct color composites of multi-band images. The small number of X-ray counts in this short observation prevents us from producing a tri-color X-ray image of NGC 5471. Table 1 summarizes the observations used for imaging and spectral analysis. Most of the adopted observations were made within one year span, so there is no significant variations of the instrumental background⁸.

The CIAO 4.2 software is used for the X-ray data calibration and spectrum extraction. We reprocess the *Chandra* data starting with the Level 1 event files following the pipeline on the official website⁹. Point-like sources in three broad bands, 0.3–1.5 keV (S), 1.5–7.0 keV (H), and 0.3–7.0 keV (B), are identified from the event maps, which are produced by merging all the available observations, following the procedure detailed in Wang (2004) using a combination of three algorithms: wavelet, sliding box, and maximum likelihood centroid fitting. The estimation of the count rate of a source is based on the number of counts within the 90% EER determined from the calibrated point-spread function (PSF) of the instrument (Jerius et al. 2000). Point-like sources detected in the three GHRs are listed in Table 2.

Different CCD chips have different responses, there-

⁷ *Chandra* Proposer’s Observatory Guide ver 12.0, Figure 4.13, available at <http://cxc.harvard.edu/proposer/POG>.

⁸ <http://cxc.harvard.edu/cal/Links/Acis/acis/Cal-prods/bkgrnd/current/>

⁹ http://cxc.harvard.edu/ciao/guides/acis_data.html

TABLE 2
PROPERTIES OF DETECTED POINT SOURCES

Source (1)	CXOU Name (2)	δ_x (") (3)	CR (cts ks ⁻¹) (4)	HR (5)	HR1 (6)	Flag (7)	MI (8)
1	J140338.65+541849.9	0.6	0.07 ± 0.02	—	—	B, S	—
2	J140341.28+541904.0	0.4	0.77 ± 0.06	−0.69 ± 0.07	0.35 ± 0.08	B, S, H	NGC5457-X50, P107
3	J140342.56+541910.5	0.5	0.12 ± 0.03	—	—	B, S	—
4	J140351.90+542149.4	0.3	0.47 ± 0.06	−0.88 ± 0.06	0.28 ± 0.13	B, S	NGC5457-X130
5	J140352.60+542210.8	0.4	0.12 ± 0.03	—	—	B, S	—
6	J140353.83+542157.2	0.3	5.24 ± 0.18	−0.48 ± 0.04	0.38 ± 0.04	B, S, H	NGC5457-X21, P110
7	J140354.30+542209.4	0.4	0.13 ± 0.03	−0.89 ± 0.13	—	B, S	NGC5457-X280
8	J140354.51+542152.0	0.5	0.08 ± 0.03	—	—	B, H	NGC5457-X243
9	J140354.84+542135.3	0.4	0.09 ± 0.02	—	—	B, S, H	—
10	J140429.21+542352.9	0.3	13.40 ± 1.60	−1.00 ± 0.00	−0.21 ± 0.11	S, B	NGC5457-X17

NOTE. — The energy bands are defined as the following: 0.3–0.7 (S1), 0.7–1.5 (S2), 1.5–3 (H1), 3–7 keV (H2), S = S1+S2, H = H1+H2, and B = S+H. Column (1): Source number. (2): *Chandra* X-ray Observatory (unregistered) source name, following the *Chandra* naming convention and the IAU Recommendation for Nomenclature (e.g., <http://cdsweb.u-strasbg.fr/iau-spec.html>). (3): Position uncertainty (1σ) calculated from the maximum likelihood centroiding and an approximate off-axis angle (r) dependent systematic error $0''.2 + 1''.4(r/8')^2$ (an approximation to Figure 4 of Feigelson et al. (2002)), which are added in quadrature. (4): On-axis source broad-band count rate — the sum of the exposure-corrected count rates in the four bands. (5–6): The hardness ratios defined as $HR = (H - S2)/(H + S2)$ and $HR1 = (S2 - S1)/S$, listed only for values with uncertainties less than 0.2. (7): Energy bands in which the source is detected, and from which the most accurate position is adopted in Column (2). (8): Matching identifiers of other X-ray catalogs: from Liu (2011, with a prefix "NGC5457-X") and from Pence et al. (2001, with a prefix "P").

TABLE 3
JOURNAL OF IR, OPTICAL AND UV DATA

Object	Observation Date	Filter	λ (Å) ^a	Bandwidth (Å) ^a	Band	Exposure (s) ^b
M101	2004 Mar. 08	Channel 1	3.6 μ m	0.75 μ m (21%)	dust & PAH	10.4
NGC 5461	1999 Mar. 23	F656N	6562	22	H α	160(1), 600(2)
	1999 Mar. 24	F547M	5454	487	Strömgren y	600(2), 100(2), 20(3)
	1999 Jun. 17	F547M	5454	487	Strömgren y	500(2)
NGC 5462	2000 Feb. 01	F656N	6562	22	H α	160(1), 600(2)
	2000 Feb. 01	F547M	5454	487	Strömgren y	600(1), 100(2), 20(2)
NGC 5471	1997 Nov. 01	F656N	6562	22	H α	180(1), 600(2)
NGC 5457	Co-added	FUV	1550	300	hot star	1500

^a The effective wavelength and bandwidth of the filters are taken from the IRAC Instrument Handbook (Fazio et al. 2004) for the *Spitzer* data, the WFPC2 Instrument Handbook (Biretta et al. 1996) for the *HST* observations and the flight calibration (Morrissey & GALEX Science 2004) for the *GALEX* images.

^b The exposure time is followed by the number of exposures in parentheses. Multiple exposures are used to remove cosmic rays.

fore, the instrumental backgrounds are subtracted from the raw event maps in four energy bands: 0.3–0.7 keV (S1), 0.7–1.5 keV (S2), 1.5–3.0 keV (H1), and 3.0–7.0 keV (H2), then the net count maps are corrected by the exposure maps of these four energy bands. The final net intensity maps (S1, S2, and H1+H2) are used to produce tri-color X-ray images, and the S1+S2 net intensity maps are used as the X-ray images in the multi-band color-composite images. Point sources have been excised from the H1+H2 intensity maps of NGC 5461 and NGC 5462, and the contours extracted from the resulting diffuse emission maps have been overplotted on the corresponding images in Figure 1.

The archival infrared (IR), optical and UV data from space telescopes are also included in this study in order to explore the physical properties of interstellar gas in various phases in and around these GHRs. The IR 3.6 μ m image is obtained with the *Spitzer* Infrared Array Camera (IRAC; PI: George Rieke). The *HST* WFPC2 images of the three GHRs are from the Cycle 6 program GO-6829 (PI: You-Hua Chu). The UV image is a stacked one from the “Tracing the Extreme Edges of Galaxies in UV and HI” program in Cycle 3 (PI: Frank Bigiel).

As we do not make photometric measurements, the post basic calibration data are used directly. Relevant information of these complementary IR, optical, and UV data is summarized in Table 3. The multiple exposures of the *HST* WFPC2 observations in each band are employed to remove cosmic rays using the IRAF tasks *xxap* and *imcombine*.

3. DATA RESULTS

3.1. Spatial Properties

To investigate the relative distributions of the IR, optical, and X-ray emission, we have used these images to produce the color composites in Figure 1 (panels *a–d*) for NGC 5461, NGC 5462, and NGC 5471. The X-ray images used in these color composites are the adaptively smoothed net intensity maps in the 0.3–1.5 keV energy band. The alignment among the multi-band images is based on the world coordinates systems (WCS) and is accurate to better than 1". To examine the hardness of the X-ray emission, we have also made tri-color composites using the adaptively smoothed net intensity maps in the 0.3–0.7, 0.7–1.5, and 1.5–7.0 keV bands for NGC 5461 and NGC 5462, shown in the panels *e* and *f* of Figure 1.

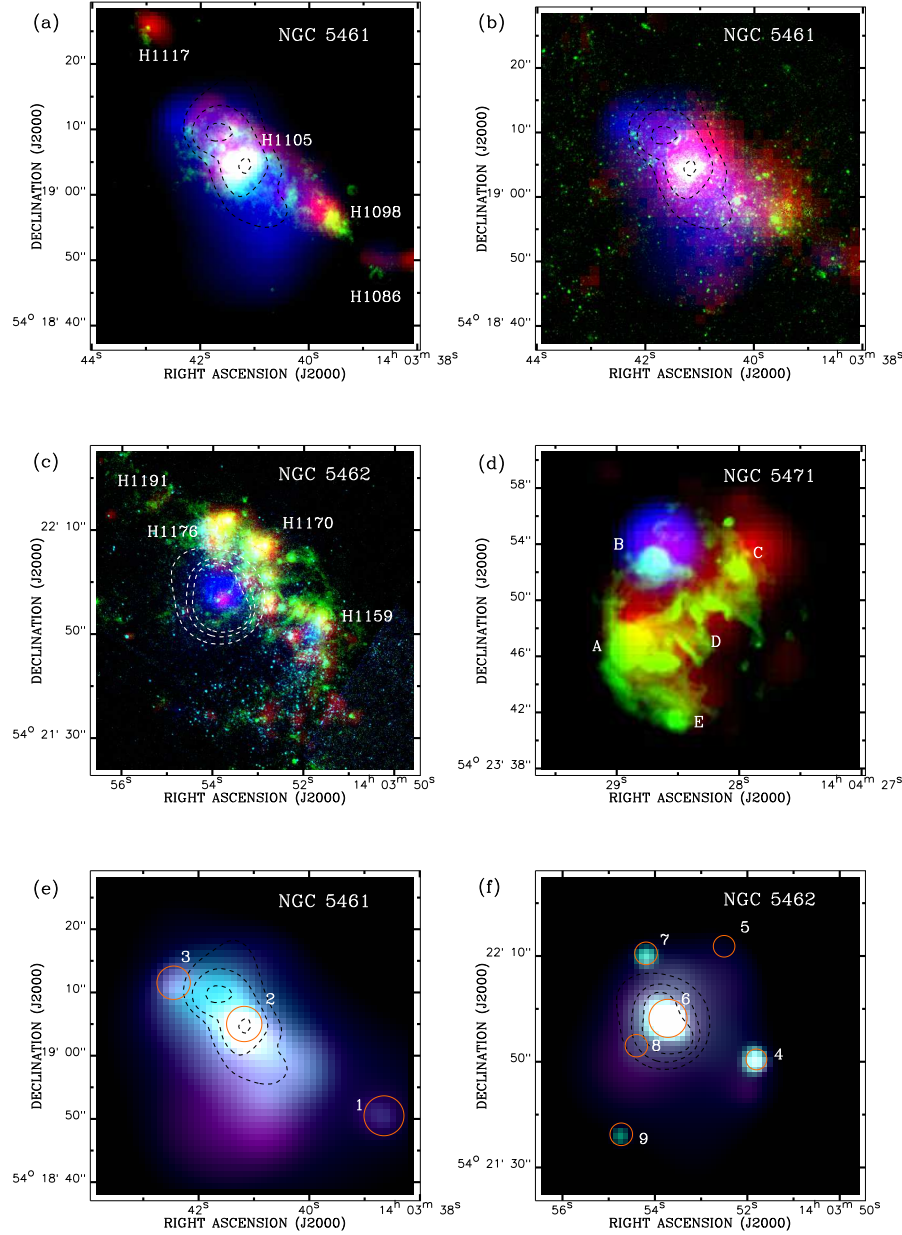


FIG. 1.— Multi-band (panels *a–d*) and tri-color X-ray (panels *e* and *f*) images of the three GHRs. The red, green, and blue colors in the multi-band images *a*, *c*, and *d* correspond to *Spitzer* IRAC 3.6 μ m, *HST* WFPC2 F656N narrow band (H α line), and *Chandra* ACIS soft (0.3–1.5 keV) band; those in panel *b* represent the Strömgren *y* (*HST* F547M), UV (*GALEX*), and X-ray (*Chandra* 0.3–1.5 keV) emission in NGC 5461; and those in the tri-color X-ray images *e* and *f* represent soft (0.3–0.7 keV), medium (0.7–1.5 keV) and hard (1.5–7.0 keV) bands, respectively, and the cyan color in panel *c* represents the Strömgren *y* (*HST* F547M) band image of NGC 5462. The orange circles in panels *e* and *f* mark the detected X-ray point sources; their radii are of 1.2 times the 90% ERR. The dashed contours overlotted on panels *a*, *b*, *e*, *f* (black), and *c* (white) represent the point-source-excised surface brightness of hard X-ray band at levels of (1.19, 1.35, and $1.68) \times 10^{-5}$ photon s $^{-1}$ cm $^{-2}$ arcmin $^{-2}$ in panels *a*, *b*, and *e*, and (1.09, 1.29, and $1.70) \times 10^{-5}$ photon s $^{-1}$ cm $^{-2}$ arcmin $^{-2}$ in panels *c* and *f*, respectively, which are 3σ , 5σ , and 9σ above the local background.

NGC 5471 has insufficient signal to warrant such color image.

3.1.1. NGC 5461

Optical images of NGC 5461 show a bright core, where a high concentration of clusters are found, and extended distribution of stars and gas to the northeast and southwest of the core, roughly along a spiral arm of M101 (Figure 2 of Chen et al. 2005). NGC 5461 is also a bright X-ray emitter (Figure 1e), and as shown in Fig-

ure 1a–b, its diffuse X-ray emission follows the distribution of stars, peaking at the bright optical core H1105 and extending to the northeast and southwest. The central X-ray emission has been identified as a quasi-soft source (Di Stefano & Kong 2004, Src. 114 therein). In the 0.3–0.7 keV band, the diffuse emission shows a remarkable deviation from the GHR’s distribution – it extends $\sim 15''$ from the southern boundary of the H α bright region southward toward a region of elevated stellar den-

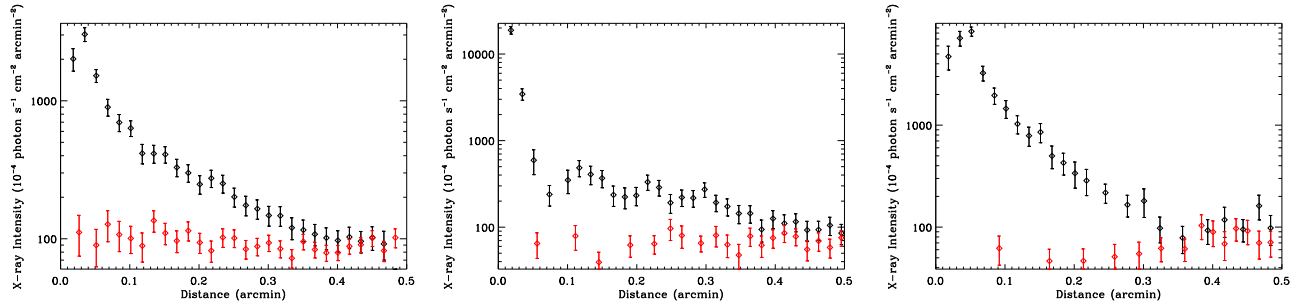


FIG. 2.— Radial surface brightness profile comparisons in the broad band (0.3–7.0 keV) to determine the diffuse extraction regions in NGC 5461 (left), NGC 5462 (middle), and NGC 5471 (right). The distance to the center in NGC 5461 is measured along the minor axes, and on- and off-source profiles are plotted in black and red data points, respectively. The extraction regions are selected to be elliptical with semi-major and minor axes of $26''25 \times 21''$ and position angle of 44° for NGC 5461, circular with a radius of $27''$ for NGC 5462, and $24''6$ for NGC 5471. The threshold count rate is listed in the first row of Table 4 reporting spectral fitting results.

sity, which is visible in both *HST* WFPC2 continuum images (Chen et al. 2005) and the *GALEX* UV image (Figure 1b). The linear scale of this soft X-ray extension is about 500 pc at the distance of M101, and is too large to be a sign of the blown out hot gas from H1105; the spectral analysis of this feature is presented in Section 3.2 and its nature is further discussed in Section 4.1.

3.1.2. NGC 5462

Optical images of NGC 5462 show that its stars are distributed roughly in the northeast-southwest direction along a spiral arm, and that the dense ionized gas (seen in H α) is offset from the stars in the downstream direction (northwest, Chen et al. 2005). The multi-band image of NGC 5462 in Figure 1c shows that the diffuse X-ray emission is also offset from the stars, but in the opposite direction to the H II gas. This relative distribution is very different from that of NGC 5461, where diffuse X-rays follow the stars and H II gas except for the soft X-ray extension to the south.

As seen in the tri-color X-ray image (Figure 1f), near the centroid of the diffuse X-ray emission is the bright X-ray point source Src. 6 (as listed in Table 2) at $[14^{\text{h}}03^{\text{m}}53^{\text{s}}.8, 54^{\circ}21'57'']$, which was identified as a black hole (BH) candidate by Mukai et al. (2003). This point source is coincident with a bright IR source (Figure 1c), and the candidate star cluster NGC 5462-19 of Chen et al. (2005). Since this point source is the dominant X-ray emitter in this field, we analyze its spectrum in Section 3.2. The non-thermal nature of its X-ray spectrum, the light absorption, and the steep photon index (see also Col. 4 in Table 4) indicate that this point source could be a BH/X-ray binary in M101 or a nearly face-on AGN in the background. Src. 6 is very different from the point source Src. 4 near H1159, which is a quasi-soft X-ray source identified by Di Stefano & Kong (2004, Src. 116 therein). The physical nature of Src. 6 will be discussed in Section 4.3.

3.1.3. NGC 5471

HST images of NGC 5471 have resolved the five knots defined by Skillman (1985), A–E, into clusters with associated H II gas (Chen et al. 2005). The multi-band image of NGC 5471 (Figure 1d) shows that the X-ray emission peaks at the B-knot. As this is a 15 ks observation, it is not clear whether faint diffuse emission is pervasive in this GHR complex. The angular size of NGC 5471B is

comparable to the equivalent radius of the PSF even in the on-axis observation, and therefore it is not surprising that NGC 5471B is identified as a point source in our and former detections (Src. 10 in Table 2). The spectral analysis of this source uses all available sections of the Ms observation of M101 to improve the signal-to-noise ratio, assuming that all X-ray emission originates from the [S II]/H α enhanced shell in NGC 5471B, as often seen in X-ray-bright superbubbles (e.g., Chu & Mac Low 1990).

3.2. X-ray Spectral Analysis

The X-ray spectra of the diffuse emission from the three GHRs are extracted from each individual observation using CIAO command *specextract*. Six, seven, and eight observations are used for NGC 5461, NGC 5462, and NGC 5471 for full coverage, respectively (see Table 1 for the data adoption). The adopted on-source spectral extraction regions are elliptical (for NGC 5461) or circular (for NGC 5462 and NGC 5471). The region sizes are determined by comparing the on-source and off-source radial surface brightness profiles, as illustrated in Figure 2. The threshold intensities are listed in the first row of Table 4, and the regions for the spectral extraction are overlaid on the raw X-ray images of NGC 5461, NGC 5462, and NGC 5471 in Figure 3. All point-like sources detected in NGC 5461 and NGC 5462 are excised with circular exclusive regions of radii 1.2 times the 90% EER, which enclose at least 95% X-ray emission from the point sources. For the intriguing X-ray source Src. 6, 11 observations are employed (Table 1) to extract its spectrum using CIAO command *psextract*. The adopted source region is circular with a radius 1.2 times the 90% EER, and the background region is a concentric annulus with radii of 1.2–2 times the 90% EER.

Since the ACIS-S3 CCD is completely filled by M101 in every segment of the Ms observation, local backgrounds for the diffuse X-rays cannot be obtained from this chip, and thus we adopt the “double background subtraction” method to account for the position dependence of the background, effective area, and energy response of the instruments. The off-source region for NGC 5461 or NGC 5462 is selected less ideally from an adjacent chip, and that for NGC 5471 is selected in the nearby field on the same chip (green dashed rectangle and polygon in Figure 3). The spectra of the non-X-ray contributions are extracted individually from the corresponding regions in the stowed background data in CALDB 4.2

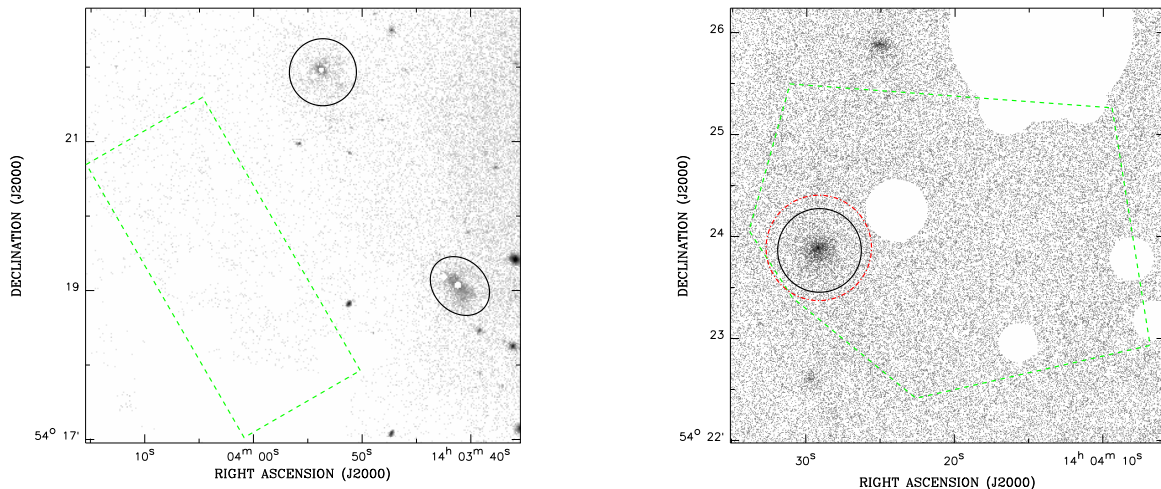


FIG. 3.— Raw images of the fields containing NGC 5461, NGC 5462 (left) and NGC 5471 (right). These are merged event maps of the ACIS observations selected to make the spectral extraction of these sources. On- and off-source extraction regions are represented in black solid circles and green dashed polygons (outside the red dash-dotted circle for NGC 5471), respectively. The background regions are compromises among the data sets of different observations.

and normalized according to the 10-12 keV count rates (Hickox & Markevitch 2006). The on- and off-source spectra extracted from different observations for each GHR are weighted by exposure and combined to improve the statistics. The net on-source and off-source spectra are jointly fitted in XSPEC.

The optically-thin thermal plasma emission model, MEKAL (Mewe et al. 1985), plus an additional non-thermal component is used to fit the spectra of the diffuse emission from the three GHRs. Based on the oxygen and iron abundances determined from optical spectrophotometry of the three GHRs (Torres-Peimbert et al. 1989; Esteban et al. 2002; Kennicutt et al. 2003), the abundance parameters in the thermal components of NGC 5461, NGC 5462, and NGC 5471B are adopted to be 0.65, 0.42, and 0.25 Z_{\odot} , respectively. The neutral hydrogen column density of the absorption to the fitting model is set to be free (while it was fixed in the analyses of Kuntz & Snowden (2010) and Wang (1999b)). The fitted spectra are shown in Figure 4. The spectral results are summarized in Table 4, in which Rows (5)-(11) give the spectral fit parameters, and Rows (12)-(14) show the derived physical parameters.

The best-fit models for the X-ray spectra of the three GHRs are all characterized by a soft thermal component (~ 0.2 keV), and a non-negligible power-law component which dominates the spectra above ~ 1.0 keV. The X-ray luminosities of the thermal component for NGC 5461, NGC 5462, and NGC 5471 are $(2.9, 1.7, \text{ and } 8.2) \times 10^{38} \text{ erg s}^{-1}$, respectively. As a comparison, Kuntz & Snowden (2010) and Wang (1999b) obtained lower luminosities. Such discrepancies may be caused by a combination of a few factors: in addition to different spectral extraction regions, larger absorbing hydrogen column densities and lower metal abundances were derived or adopted in our spectral fittings. It seems that these M101 GHRs are the most luminous in X-rays among the known GHRs in the local universe. This high

X-ray luminosity will be discussed in Section 4.

We choose to use a power-law component to fit the hard tails in the spectra, instead of assuming another thermal component of higher temperature as Kuntz & Snowden (2010) did, because the power-law component may better represent the contribution from unresolved point sources, residual emission of the excluded point sources (in NGC 5462), and even emission from cosmic rays at shocks of stellar winds and SNRs.

The point source CXOJ140353.83+542157.2 (Src. 6) is characterized by a power-law spectrum of intrinsic luminosity $\sim 2.7 \times 10^{38} \text{ erg s}^{-1}$ in the 0.5-5.0 energy band for the M101 distance of 6.8 Mpc. Given that the excluded region encircles $\gtrsim 90\%$ energy, the residual X-ray luminosity of the excluded point source in the diffuse emission of NGC 5462 may be up to $\sim 10^{37} \text{ erg s}^{-1}$. This source (Src. 6) is at least ten times brighter than the other detected point sources except for the central emissions in NGC 5461 and NGC 5471B, which are detected as two point sources (see Table 2). Therefore, the contributions of point sources in the spectra of diffuse emission in the three GHRs may be at least $\sim 10^{37} \text{ erg s}^{-1}$, and are partly responsible for the power-law components in best-fit models.

The estimated hydrogen density of the hot gas, n_H (given in Table 4), depends on its volume. The emission region of NGC 5461 is irregular, and we assume that the elliptical extraction region represents a prolate ellipsoid and use the volume of the ellipsoid enclosed by the contour at 20% of the peak surface brightness for the hot gas. The hot gas volume in NGC 5462 is determined with the same assumptions. The spectral extraction region of NGC 5471B (Figure 3) is much larger than its optical size due to the large scattering of X-ray photons; thus, we assume that the diffuse X-ray emission originates from the interior of the [S II]/H α -enhanced shell in NGC 5471B (Chen et al. 2002), which is reasonable for a superbubble or a hypernova remnant scenario. Conse-

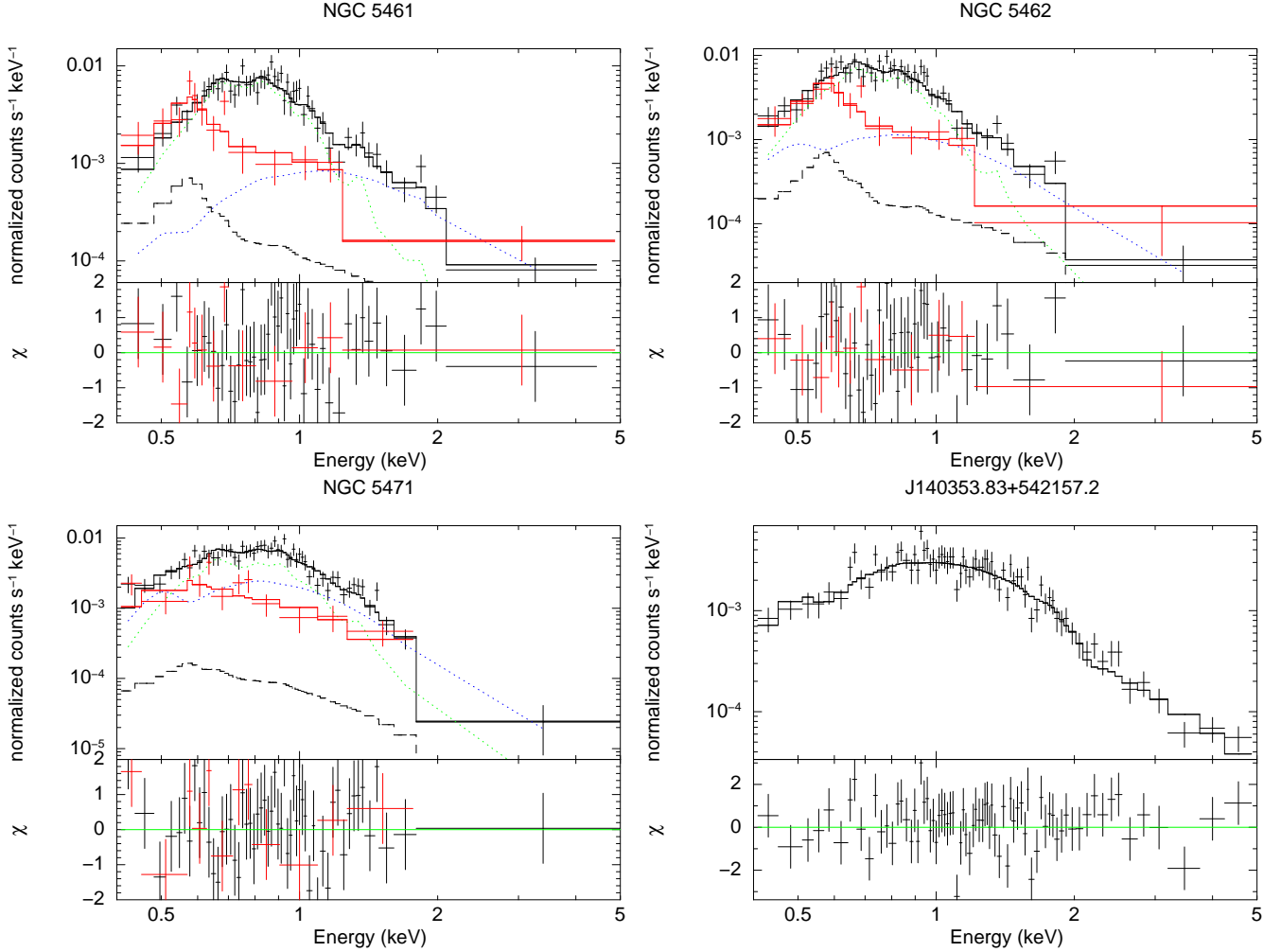


FIG. 4.— X-ray spectral analysis of NGC 5461 (top-left), NGC 5462 (top-right), NGC 5471 (bottom-left) and the point source CXO J140353.83+542157.2 (Src. 6) near NGC 5462 (bottom-right). The on- and off-source spectra are plotted in black and red colors, respectively. In the spectra of the GHRs, dotted lines represent thermal (green) and non-thermal (blue) contributions, and black dashed lines represent the diffuse background emissions which are scaled from the off-source spectra. The best-fit model of Src. 6 is a power-law, while the spectra of the three GHRs are well fitted with a MEKAL (dotted green) plus power-law (dotted blue) model. The spectral fit parameters are given in Table 4.

quently, we adopt the optical shell volume for the hot gas in NGC 5471B. A volume filling factor f is introduced to account for the fact that the emitting volume may be smaller than the assumed volume.

4. DISCUSSION

The X-ray luminosities of NGC 5461, NGC 5462, and NGC 5471 are at least an order of magnitude higher than that of 30 Dor. While the $H\alpha$ luminosities of these three M101 GHRs are also about an order of magnitude higher than that of 30 Dor, the high X-ray luminosities are not a direct consequence of the high $H\alpha$ luminosities. As shown by Chen et al. (2005), the three M101 luminous GHRs have multiple clusters at different evolutionary stages with ages ranging from <5 Myr to >10 Myr; furthermore, many clusters are as massive as the R136 cluster in 30 Dor. The diffuse X-ray luminosity of hot gas generated by a cluster is time-dependent, and grows by almost two orders of magnitude at ages of 3–10 Myr when massive O stars explode as SNe (Oskinova 2005). Therefore, the high diffuse X-ray luminosities of the three M101 GHRs are caused by the large number of

massive clusters at ages when SN explosions are rampant. Below, we discuss possible mechanisms for generating the hot gas in these GHRs.

4.1. Superbubble Scenario of the GHRs

The X-ray emission associated with GHRs NGC 5461, NGC 5462, and NGC 5471 in M101 may be produced by similar processes as in superbubbles in the Magellanic Clouds (Chu & Mac Low 1990; Wang & Helfand 1991; Wang et al. 1991). Their soft appearances and luminosities are also as expected from the quasi-spherical superbubble model with a central stellar cluster with mass of $\sim 10^5 M_\odot$ (Chu et al. 1995; Silich et al. 2005). However, the various spatial distributions of hot gas are not totally confined in visible superbubbles.

At the southern outskirts of NGC 5461, where the soft X-ray emission extends, a bright patch of UV emission is present (see Figure 1b), corresponding to the blue stars distributed in a triangular region that is clearly seen in the color composite of the *HST* WFPC2 images of Chen et al. (Figure 2, 2005). The main body of NGC 5461 stretches along a spiral arm, while the afore-

TABLE 4
X-RAY SPECTROSCOPY OF EMISSION FROM GIANT H II REGIONS

Emission Component	NGC 5461	NGC 5462	Src. 6	NGC 5471B
(1) Threshold Count Rate ^a (10^{-6} sbu)	2.67 ± 0.53	16.3 ± 3.7	...	2.14 ± 0.56
(2) Accumulated effective exposure (ks)	228.9	238.5	381.3	276.6
(3) Net Count Rate ^b (10^{-3} cts s^{-1})	4.6 ± 0.2	4.3 ± 0.2	3.6 ± 0.1	4.5 ± 0.1
(4) Adopted Abundance for MEKAL part (Z_{\odot})	0.65	0.42	...	0.25
(5) Neutral Hydrogen Column Density (10^{22} cm^{-2})	$0.3^{+0.2}_{-0.2}$	$0.2^{+0.2}_{-0.1}$	$0.26^{+0.05}_{-0.05}$	$0.3^{+0.1}_{-0.2}$
(6) Temperature of MEKAL Component (keV)	$0.25^{+0.06}_{-0.06}$	$0.24^{+0.04}_{-0.06}$...	$0.19^{+0.08}_{-0.04}$
(7) Photon Index	$2.4^{+0.9}_{-0.8}$	$3.5^{+1.8}_{-1.1}$	$3.1^{+0.2}_{-0.2}$	$5.6^{+1.0}_{-0.8}$
(8) Emission Measure/ $d_{6.8}^2$ (10^{62} cm^{-3})	$0.3^{+1.2}_{-0.2}$	$0.2^{+1.7}_{-0.1}$...	$2.6^{+5.4}_{-2.1}$
(9) A_{Γ} (10^{-5} photons keV^{-1} cm^{-2} s^{-1} at 1 keV)	$0.3^{+0.2}_{-0.2}$	$0.3^{+0.3}_{-0.1}$	$1.7^{+0.3}_{-0.2}$	$1.4^{+0.6}_{-0.4}$
(10) $\chi^2/\text{degrees of freedom}$	54.0/52	51.4/48	87.5/77	69.5/57
(11) $F_{X,MEKAL}/F_{X,PL}$ ^c	1.8	2.5	...	1.5
(12) $L_{X,0.5-5.0}$ keV^d (10^{38} erg s^{-1})	2.9	1.7	2.7	8.2
(13) $n_H/f^{-1/2}d_{6.8}^{-1/2}$ (cm^{-3}) ^e	0.29	0.014	...	8.0
(14) $E_{th}/f^{1/2}d_{6.8}^{5/2}$ (10^{52} ergs) ^f	9.1	161.	...	2.9

NOTE. — See Section 3.2 and lower notes for the descriptions of each row. The errors of the count rates are Poissonian, and the confidence ranges of the fitted parameters are at the 90% level.

^a The count rates are counted in 0.3–7.0 keV energy interval without background subtraction, which are summarized from surface brightness profile analyses. 1 sbu = 1 cts cm^{-2} s^{-1} $arcsec^{-2}$.

^b The net count rates are counted in 0.4–5.0 keV energy interval with instrumental background subtraction, and the emissions from point-like sources (Src. 1–9 in Table 2) have been excluded from the GHRs' diffuse emissions.

^c Model absorbed flux ratio of MEKAL to power-law of 0.5–5.0 keV.

^d Unabsorbed X-ray luminosity. Calculated from fitted model flux, for those three GHRs only the MEKAL part is included.

^e Root mean square (RMS) hydrogen density generated from the best-fit normalization parameter of the MEKAL model, where f denotes filling factor of the hot gas, the ellipsoids for H1105 (with half-axes $3''.15 \times 3''.15 \times 5''.3$, size of contour at 20% of the top value) and NGC 5471B (with half-axes $1''.1 \times 0''.85 \times 0''.85$; size of the [S II]/H α -enhanced shell), and the sphere for NGC 5462 (with radius $0''.45$) are assumed, and the He/H ratio are 0.09, 0.09, 0.08 for H1105, NGC 5462 and NGC 5471B, respectively.

^f The thermal energy of the hot plasma is calculated as: $E_{th} = V \cdot f \cdot u_X = \frac{3}{2} \cdot 2.3n_H kT \cdot V \cdot f$, where n_H is the hydrogen density of shocked gas.

mentioned region of blue stars is detached from the main body and located in the upstream side, possibly belonging to an earlier episode of star formation triggered by the spiral density wave. The luminosity of the extended soft X-ray emission is of order 10^{37} erg s^{-1} , if an absorbed thermal emission model with $N_H \sim 10^{21}$ cm^{-2} and $kT \sim 0.2$ keV is adopted. This X-ray luminosity is too high to be accounted for solely by the stellar emission from the unresolved OB-stars and active pre-main sequence stars that also contribute to the UV emission. This soft diffuse X-ray emission most likely originates from hot gas powered by SN explosions and fast stellar winds. It is unlikely that outflows from the clusters in H1105 are responsible for this hot gas because of the following reason. If the hot gas moves at its isothermal sound velocity ~ 100 km s^{-1} , it would take 5 Myr to reach a distance of 500 pc, the outer boundary of the diffuse X-ray emission. As the clusters in H1105 are all < 5 Myr old (Chen et al. 2005), it is impossible for them to have produced hot gas through SN explosions 5 Myr ago. A better candidate for producing this hot gas is the star cloud, i.e., high surface density of stars over an extended area, between H1105 and H1098, directly due north of the diffuse soft X-ray emission and best seen in the color image of Chen et al. (2005). This star cloud is reminiscent of the stellar content in supergiant shells (SGSs), such as SGSs LMC-3 and LMC-4, where diffuse soft X-ray emission is detected with X-ray luminosities

of 10^{37} erg s^{-1} (Points et al. 2001). It is possible that the outflow of hot gas produced by energy feedback of this star cloud contributes to the southern extension of diffuse soft X-ray emission.

In NGC 5462, the large displacement of the diffuse X-ray emission from the H II regions indicates that the current young clusters embedded in the H II regions are not likely responsible for generating the required X-ray-emitting hot gas. On the other hand, the diffuse X-ray emission is better coincident with the ridge of older blue stars that are parallel to the H II regions and offset in the same direction as the diffuse X-ray emission. It is possible that SN explosions from these stars power the X-ray emission. The H α image of NGC 5462 (Figure 6e of Chen et al. 2005) shows long filaments extending from the ridge of blue stars toward the diffuse X-ray emission region, further supporting the hot gas outflow scenario.

It should be noted that quiescent superbubbles (not energized by recent SN explosions; Chu et al. 1995) associated with the sub-H II regions in NGC 5462 would not be detected by even the 1 Ms *Chandra* observation, whose detection limit for point sources is several $\times 10^{36}$ erg s^{-1} . Superbubbles' soft X-ray emission can also be absorbed by surrounding dense cold medium and become undetectable. This may explain the apparent absence of X-ray emission associated with H1170. Only X-ray-bright superbubbles may be detected by the Ms *Chandra* observation, and they appear as soft or quasi-soft sources,

such as Src. 4 in H1159.

The spatial analysis of X-rays in NGC 5471B is limited by the short exposure of the on-axis observation. The angular size of B-knot is too small to be resolved in the *Chandra* observation, and the potential contribution from other knots of NGC 5471 to the total luminosity cannot be excluded. The analysis of high-dispersion echelle spectra of the H α line indicates that only the B-knot is a LVWS source (FWHM $\gtrsim 120$ km s $^{-1}$, Sun et al., in preparation), which is unique within NGC 5461 and NGC 5471. In the next section we discuss NGC 5471B as a hypernova remnant.

4.2. NGC 5471B as Hypernova Remnant

The broad H α velocity profile of NGC 5471B suggests that an energetic explosive event has taken place. If the large velocities originate from an expanding shell, the extreme velocity offsets of the wings of the broad velocity profile indicate an expansion velocity at least 300 km s $^{-1}$. If the temperature T_X measured from the MEKAL model is adopted as the average temperature $\langle T \rangle$ weighted by emission measure, which is 1.27 times the postshock temperature T_s based on the numerical calculations of the Sedov-Taylor self-similar solution, we can then estimate the blast wave velocity as ~ 340 km s $^{-1}$, which is consistent with the value obtained by Chen et al. (2002). We adopt the size of the remnant as that of the [S II]/H α -enhanced shell, and derive the atomic number density of ambient medium from the RMS hydrogen density (Row 12 in Table 4) under the assumption that the filling factor is of unity. Based on the Sedov solution, we then estimate the remnant age as 3.4×10^4 yr, and the explosion energy as 1.5×10^{52} ergs, comparable on order of magnitude to the thermal energy E_{th} (Table 4) and consistent with the “hypernova remnant” scenario (Wang 1999a).

The remnant age is smaller than the typical time scale for it to enter the pressure-driven snowplow (PDS) phase (Cioffi et al. 1988):

$$t_{PDS} \sim 2.2 \times 10^4 E_{52}^{3/14} n_0^{-4/7} \zeta_m^{-5/14} \text{ yr}, \quad (1)$$

where E_{52} is the expansion energy in units of 10^{52} ergs, n_0 is the atomic number density of ambient medium, and ζ_m is relative metallicity to solar abundance employed in the cooling function. In the case of NGC 5471B, $t_{PDS} \simeq 4.2 \times 10^4$ yr, which is consistent with the Sedov-Taylor phase assumption; meanwhile, the isothermal phase starts at radius:

$$R_{PDS} = 33.0 E_{52}^{2/7} n_0^{-3/7} \zeta_{m,0.25}^{-1/7} \text{ pc}, \quad (2)$$

which is comparable to the apparent size of NGC 5471B in the H α and [S II] images.

For comparison, the quiescent superbubble model (Chu et al. 1995) would produce unphysical parameters. In such a scenario, the temperature and density distributions in the shocked wind layer of an energy-conserving bubble are

$$n(x) = n_c(1-x)^{-2/5}, \quad T(x) = T_c(1-x)^{2/5}, \quad (3)$$

where $x = r/R$ is the fractional radius, R is the radius of the bubble:

$$R = 42 L_{37}^{1/5} n_0^{-1/5} t_6^{3/5} \text{ pc}, \quad (4)$$

n_c and T_c are the central density and temperature:

$$n_c = 1.1 \times 10^{-2} L_{37}^{6/35} n_0^{19/35} t_6^{-22/35} \text{ cm}^{-3}, \quad (5)$$

$$T_c = 0.27 L_{37}^{8/35} n_0^{2/35} t_6^{-6/35} \text{ keV}, \quad (6)$$

where L_{37} is the mechanical luminosity of the stellar winds measured in units of 10^{37} erg s $^{-1}$, n_0 is the atomic number density of the ambient medium in units of cm $^{-3}$, and t_6 is the age of the bubble in 10^6 yr.

Adopting the same definition of the dimensionless temperature $\tau = T_{\min}/T_c$ as in Chu et al. (1995), where $T_{\min} = 5 \times 10^5$ K is the minimum temperature of the hot gas that will emit in soft X-ray band, and assuming the measured X-rays represent the hot gas from the interior of a spherical bubble with radius of 30 pc, the average size of the [S II]/H α -enhanced shell, the volume emission measure of the hot gas in NGC 5471B can be expressed as

$$\begin{aligned} EM &= \int n_e n_H d^3r \\ &= 2.3 \times 10^{60} n_c^2 I(\tau) \text{ cm}^{-3}, \end{aligned} \quad (7)$$

where n_c is in units of cm $^{-3}$, and the dimensionless integral is $I(\tau) = (125/33) - 5\tau^{1/2} + (5/3)\tau^3 - (5/11)\tau^{11/2}$; meanwhile, the observed temperature is the average temperature:

$$\langle T \rangle = \frac{\int n(r)^2 T(r) d^3r}{\int n(r)^2 d^3r} = T_c K(\tau) / I(\tau), \quad (8)$$

where $K(\tau) = (125/156) - (5/13)\tau^{13/2} + (5/4)\tau^4 - (5/3)\tau^{3/2}$. Therefore, substituting the radius of bubble R , the emission measure and the temperature of the hot gas to equations 4, 7, and 8, the derived mechanical luminosity of winds is 1.3×10^{38} erg s $^{-1}$, the atomic number density of ambient medium is several of 10^6 cm $^{-3}$, and the age of the bubble is 41 Myr.

If the candidate clusters NGC 5471-10 and 11 are massive evolved ones, $M_c \sim 10^4 M_\odot$, $t_{10} \gtrsim 20$ Myr and $t_{11} \gtrsim 60$ Myr, as seen in the color-magnitude diagram (Chen et al. 2005, Figure 10 therein), the mechanical luminosity and the bubble age are consistent; however, the ISM density is not physical. Therefore, the “hypernova remnant” scenario is more favorable compared to the superbubble model.

4.3. Physical Properties of Src. 6 in NGC 5462

The bright X-ray point source Src. 6 near the centroid of the diffuse emission in NGC 5462 has a spectrum that is best described by a power-law model. Src. 6 has been proposed to be a BH/X-ray binary (P110 of Mukai et al. 2003). The coincidence between this BH/X-ray binary candidate and a previously identified optical cluster candidate (NGC 5462-19 of Chen et al. 2005) appears to suggest that the X-ray binary is a member of the cluster; however, a re-visit of the IR observations, optical and radio images raises doubt about this picture.

Bright IR emission is not expected from a BH/X-ray binary, yet *Spitzer* observations detected a bright IR counterpart of Src. 6. The spectral energy distribution (SED) of the optical and IR emission from this source (see Figure 5) suggests the existence of heated dust. This

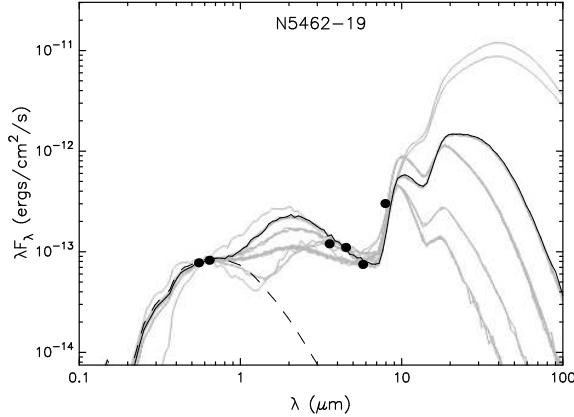


FIG. 5.— Spectral energy distribution (SED) fitting of Src. 6 in the field of NGC 5462. The 6 data points from the blue to red wings are of Strömgren y (*HST* F547M), WFPC2 R (*HST* F675W), *Spitzer* IRAC 3.6 μ m, 4.5 μ m, 5.8 μ m, and 8.0 μ m bands, respectively. The dashed line represents the SED of a simple single population, which cannot fit the mid-IR excess; and the black and gray solid ones are scaled young stellar object (YSO) models which are not relevant here since this point source is too bright to be a YSO at the distance of M101. Therefore, this candidate cluster is more likely to be a background star-forming galaxy with a strong X-ray source if the detected sources all coincide.

SED is inconsistent with that of young stellar objects (YSOs) in both spectral shapes and luminosities. It is, however, similar to those frequently seen in active galactic nuclei (AGN). If the minimum at the 5.8 μ m band corresponds to the rest-frame minimum at the 4.5 μ m band (due to the presence of PAH emission in the adjacent bands) seen in star-forming regions or galaxies, this source is likely a background AGN at $z \sim 0.3$. The small absorption column implied by the best model fit to the X-ray spectrum can be reconciled if the AGN is viewed face-on.

We examined the optical images of the cluster candidate #19 more closely. The closeup *HST* F547M image of NGC 5462-19 in Figure 6 shows a core and a diffuse halo, and it could be decomposed as a central point source and an exponential disk in GALFIT (Peng et al. 2010). This morphology is consistent with that of an AGN in a disk galaxy. If the diffuse optical emission originates from a galactic disk, the scale length of the exponential disk, as 0''.2, implies a distance of several of 10^9 pc since the scale length is around 1 to 10 kpc for most disk galaxies. This estimated distance is of the same order of magnitude as the redshift distance estimated crudely from the IR SED. For a distance of 10^9 pc, the intrinsic X-ray luminosity of Src. 6 would be $\sim 10^{43}$ erg s $^{-1}$, within the X-ray luminosity range of AGN (Allevato et al. 2011). Another important clue to the nature of Src. 6 is provided by its coincidence with the radio source NGC 5457E- θ (Eck et al. 2002), which definitively indicates that Src. 6 is a radio loud AGN rather than a BH/X-ray binary. We therefore conclude that Src. 6 originates from the background AGN, instead of a BH/X-ray binary in a candidate cluster.

5. CONCLUDING COMMENTS

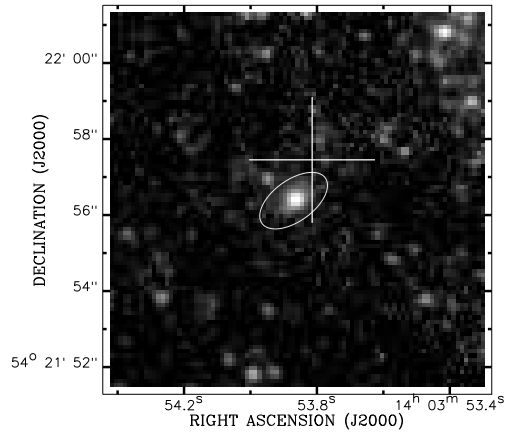


FIG. 6.— Close-up view of the cluster candidate NGC 5462-19 (Chen et al. 2005) in *HST* F547M band. The white ellipse represents the exponential disk from the GALFIT decomposition result with a radius of 5 times of the scale length, and the white cross indicates the location of the X-ray detected source (Src. 6).

Giant H II regions contain high concentrations of massive stars; therefore, they are excellent laboratories to study modes of massive star formation and subsequent evolution. We have analyzed *Chandra* observations of X-ray emission from three GHRs in M101, NGC 5461, NGC 5471 and NGC 5462. The X-ray emission from these three GHRs exhibits diverse properties with respect to the individual H II regions and associated stellar clusters.

Our main results are the following:

1. The spectra of diffuse X-ray emission from NGC 5461, NGC 5462, and NGC 5471B all appear to be thermal with characteristic plasma temperatures ~ 0.2 keV, although contributions from point sources may be significant and are modeled as an additional power-law component. The luminosities of the thermal components of the GHRs are: 2.9×10^{38} , 1.7×10^{38} , and 8.2×10^{38} erg s $^{-1}$ for NGC 5461, NGC 5462, and NGC 5471B, respectively, which represent emission from hot gas commonly generated in massive star-forming regions. They are very luminous because they contain multiple massive clusters and star clouds at different ages and some of them are ripe with rampant SN explosions.
2. The distributions of diffuse X-ray emission in the three GHRs exhibit distinct features. In NGC 5461, the brightest diffuse X-ray emission roughly follows the distribution intense star formation; in addition, a patch of diffuse soft X-rays extend southward over ~ 500 pc and may be attributed to outflows from the star cloud between H1105 and H1098. In NGC 5462, the extended X-ray emission is displaced from the H II regions and a ridge of blue stars; the H α filaments extending from the ridge of star cloud to the diffuse X-ray emission region suggests that hot gas outflows have occurred. In NGC 5471, the X-ray emission is very much confined within the B-knot, and our analysis indicates that the physical properties of the X-ray emitter are more consistent with a “hypernova remnant” scenario than a superbubble model. It is nevertheless unclear whether the explosion energy is pro-

vided by a single “hypernova” or concentrated multiple core-collapse SNe from a cluster.

3. The point source Src. 6 in NGC 5462 is most likely a background AGN at a distance of order of 10^9 pc and its intrinsic X-ray luminosity is $\sim 10^{43}$ erg s $^{-1}$.

We thank the anonymous referee for her/his care-

ful reading and insightful suggestions. YC acknowledges support from the 973 Program grant 2009CB824800 and the NSFC grants 11233001 and 10725312. YHC acknowledges the support of SAO/CXC grant GO0-11025X. We also thank Bing Jiang for her assistance in data reduction, and Qiusheng Gu for helpful comments on the SED of NGC5462-19.

REFERENCES

- Allevato, V., Finoguenov, A., Cappelluti, N., Miyaji, T., Hasinger, G., et al. 2011, *ApJ*, 736, 99
- Biretta, J., Ritchie, C., Baggett, S., & MacKenty, J. 1996, *Wavelength/Aperture Calibration of the WFPC2 Linear Ramp Filters*, Tech. rep.
- Brandl, B. R. 2005, in *Astrophysics and Space Science Library*, Vol. 329, *Starbursts: From 30 Doradus to Lyman Break Galaxies*, ed. R. de Grijs & R. M. González Delgado, 49–+
- Chen, C., Chu, Y., Gruendl, R., Lai, S., & Wang, Q. D. 2002, *AJ*, 123, 2462
- Chen, C., Chu, Y., & Johnson, K. E. 2005, *ApJ*, 619, 779
- Chu, Y., & Kennicutt, Jr., R. C. 1986, *ApJ*, 311, 85
- Chu, Y.-H., Chang, H.-W., Su, Y.-L., & Mac Low, M.-M. 1995, *ApJ*, 450, 157
- Chu, Y.-H., & Mac Low, M.-M. 1990, *ApJ*, 365, 510
- Cioffi, D. F., McKee, C. F., & Bertschinger, E. 1988, *ApJ*, 334, 252
- Di Stefano, R., & Kong, A. K. H. 2004, *ApJ*, 609, 710
- Eck, C. R., Cowan, J. J., & Branch, D. 2002, *ApJ*, 573, 306
- Esteban, C., Peimbert, M., Torres-Peimbert, S., & Rodríguez, M. 2002, *ApJ*, 581, 241
- Fazio, G. G., Hora, J. L., Allen, L. E., Ashby, M. L. N., Barmby, P., et al. 2004, *ApJS*, 154, 10
- Feast, M. W., Thackeray, A. D., & Wesselink, A. J. 1960, *MNRAS*, 121, 337
- Feigelson, E. D., Broos, P., Gaffney, III, J. A., Garmire, G., Hillenbrand, L. A., Pravdo, S. H., Townsley, L., & Tsuboi, Y. 2002, *ApJ*, 574, 258
- Hickox, R. C., & Markevitch, M. 2006, *ApJ*, 645, 95
- Hodge, P. W., Gurwell, M., Goldader, J. D., & Kennicutt, Jr., R. C. 1990, *ApJS*, 73, 661
- Hunter, D. A., Baum, W. A., O’Neil, Jr., E. J., & Lynds, R. 1996, *ApJ*, 456, 174
- Israel, F. P., Goss, W. M., & Allen, R. J. 1975, *A&A*, 40, 421
- Jerius, D., Donnelly, R. H., Tibbetts, M. S., Edgar, R. J., Gaetz, T. J., Schwartz, D. A., Van Speybroeck, L. P., & Zhao, P. 2000, in *Society of Photo-Optical Instrumentation Engineers (SPIE) Conference Series*, Vol. 4012, *Society of Photo-Optical Instrumentation Engineers (SPIE) Conference Series*, ed. J. E. Truemper & B. Aschenbach, 17–27
- Kennicutt, Jr., R. C. 1984, *ApJ*, 287, 116
- Kennicutt, Jr., R. C., Bresolin, F., & Garnett, D. R. 2003, *ApJ*, 591, 801
- Kuntz, K. D., & Snowden, S. L. 2010, *ApJS*, 188, 46
- Liu, J. 2011, *ApJS*, 192, 10
- Mewe, R., Gronenschild, E. H. B. M., & van den Oord, G. H. J. 1985, *A&AS*, 62, 197
- Morrissey, P., & GALEX Science. 2004, in *Bulletin of the American Astronomical Society*, Vol. 36, *American Astronomical Society Meeting Abstracts*, 1385–+
- Mukai, K., Pence, W. D., Snowden, S. L., & Kuntz, K. D. 2003, *ApJ*, 582, 184
- Oskinova, L. M. 2005, *MNRAS*, 361, 679
- Pellerin, A. 2006, *AJ*, 131, 849
- Pence, W. D., Snowden, S. L., Mukai, K., & Kuntz, K. D. 2001, *ApJ*, 561, 189
- Peng, C. Y., Ho, L. C., Impey, C. D., & Rix, H.-W. 2010, *AJ*, 139, 2097
- Points, S. D., Chu, Y.-H., Snowden, S. L., & Smith, R. C. 2001, *ApJS*, 136, 99
- Saha, A., Thim, F., Tammann, G. A., Reindl, B., & Sandage, A. 2006, *ApJS*, 165, 108
- Schaerer, D., & de Koter, A. 1997, *A&A*, 322, 598
- Silich, S., Tenorio-Tagle, G., & Añorve-Zeferino, G. A. 2005, *ApJ*, 635, 1116
- Skillman, E. D. 1985, *ApJ*, 290, 449
- Torres-Peimbert, S., Peimbert, M., & Fierro, J. 1989, *ApJ*, 345, 186
- Townsley, L. K., Broos, P. S., Feigelson, E. D., Brandl, B. R., Chu, Y., Garmire, G. P., & Pavlov, G. G. 2006, *AJ*, 131, 2140
- Tüllmann, R., Gaetz, T. J., Plucinsky, P. P., Long, K. S., Hughes, J. P., et al. 2008, *ApJ*, 685, 919
- Tüllmann, R., Long, K. S., Pannuti, T. G., Winkler, P. F., Plucinsky, P. P., et al. 2009, *ApJ*, 707, 1361
- Wang, Q., Hamilton, T., Helfand, D. J., & Wu, X. 1991, *ApJ*, 374, 475
- Wang, Q., & Helfand, D. J. 1991, *ApJ*, 373, 497
- Wang, Q. D. 1999a, *ApJ*, 517, L27
- . 1999b, *ApJ*, 510, L139
- . 2004, *ApJ*, 612, 159
- Yang, H., Skillman, E. D., & Sramek, R. A. 1994, *AJ*, 107, 651